Conservative Full-Potential Calculations for Axisymmetric, Transonic Flow

Lawrence L. Green* and Jerry C. South Jr.†
NASA Langley Research Center, Hampton, Virginia

A conservative, finite difference, full-potential relaxation code has been developed to solve transonic flow around axisymmetric or nonlifting, planar, two-dimensional bodies. The program utilizes the artificial compressibility method to provide an upwind bias in supersonic regions. Calculated examples include a wide variety of axisymmetric and planar two-dimensional shapes with various blunt, pointed, and open ends in subsonic, transonic, and low supersonic freestreams. Comparisons between conservative and nonconservative full-potential calculations show perfect agreement at convergence when the flow is entirely subsonic. Noticeable differences exist, however, between the conservative and nonconservative solutions for transonic flows with shocks.

Introduction

IN 1973, South and Jameson[1] presented a method for numerical analysis of axisymmetric transonic flow past bodies of rather general meridian shapes. The method employed a line relaxation scheme for iterative solution of the full-potential difference equation in nonconservative form. A subsequent version of the method, which allows coordinate inputs for the body shape, has been widely distributed as the RAXBOD[2] code.

Although many useful transonic potential codes developed in the early 1970's were nonconservative, there is increasing evidence that the conservative form is more desirable, particularly when interacted with a viscous boundary-layer method. Melnik[3] has given convincing demonstrations that, when the viscous-inviscid interactions are done correctly, the use of the conservative inviscid solution gives better agreement with experimental results than does use of the nonconservative. Aside from that, since the full-potential equation represents the conservation of mass, it is generally felt that the conservation law form should be used when shocks are captured, for it is supported by Lax's well-founded theory of weak solutions of conservation laws.[4] A graphic demonstration of the difference between solutions computed by both conservative and nonconservative schemes was given by Newman and South,[5] wherein it was seen that the nonconservative scheme produces sources of mass along the shock waves, caused by switching from upwind to central differencing without using a proper transition operator.

For some time there has been a need for a conservative version of RAXBOD. The so-called artificial compressibility method, developed in 1978 by Holst[6] and Hafez et al.,[7] provides a convenient method for implementing the conservative scheme. This paper outlines this approach; additional options have been added to the basic RAXBOD structure to allow a wider variety of meshes and body shapes and to include planar two-dimensional flow.

Presented as Paper 81-1204 at the AIAA 14th Fluid and Plasma Dynamics Conference, Palo Alto, Calif., June 23-25, 1981; submitted July 13, 1981; revision received Jan. 26, 1983. This paper is declared a work of the U.S. Government and therefore is in the public domain.

*Aero-Space Technologist, Theoretical Aerodynamics Branch, Transonic Aerodynamics Division. Member AIAA.

†Head, Theoretical Aerodynamics Branch, Transonic Aerodynamics Division. Associate Fellow AIAA.

Problem Formulation

Axisymmetric Continuity Equation

The mass conservation law governing steady transonic flows around axisymmetric bodies is

$$(\rho ur)_S + (\rho vrh)_N = 0 \tag{1}$$

in body-normal coordinates. Here u and v are the components of velocity in the tangential and normal directions, respectively. These velocity components are functions of the freestream velocity and a disturbance potential ϕ. The isentropic density is ρ, which is a function of the freestream Mach number, M_∞; the local speed, q; and the ratio of specific heats, γ. The radial distance from the axis of symmetry is r and h is the metric of the body-normal coordinate transformation. Partial derivatives with respect to the tangential and normal directions are denoted by subscripts S and N, respectively.

Generalized Continuity Equation

For several reasons, it is more convenient to express Eq. (1) in a more general form. First, for certain bodies, a sheared (body-fitting) cylindrical coordinate system can be used in place of, or in combination with, the body-normal coordinate system to provide better discretization of the problem. Figure 1 shows an example of the combined mesh, chosen to exaggerate the shearing. Second, the problem in infinite physical space is actually solved on a finite computational space having coordinates X and Y, which are related to the physical coordinates through one-dimensional "stretching" transformations. Third, the program utilizes the artificial compressibility method[7] to stabilize calculations in supersonic regions, which shifts the density evaluation upstream of the point in question. Lastly, nonlifting, planar, two-dimensional bodies can be analyzed as well as axisymmetric shapes if the cylindrical radius is replaced by unity for the planar two-dimensional cases.

Because of the possible combined body-normal and sheared grids, it is convenient to introduce a set of generalized physical coordinates ξ and η. The coordinates ξ and η are, respectively, parallel and perpendicular to a reference body shape. The reference body shape coincides with the actual shape in body-normal portions of the grid, but is a cylinder in sheared regions of the mesh. The coordinate η is always zero at the actual body surface and at the symmetry line in the sheared coordinates. Thus, the coordinates ξ and η have the

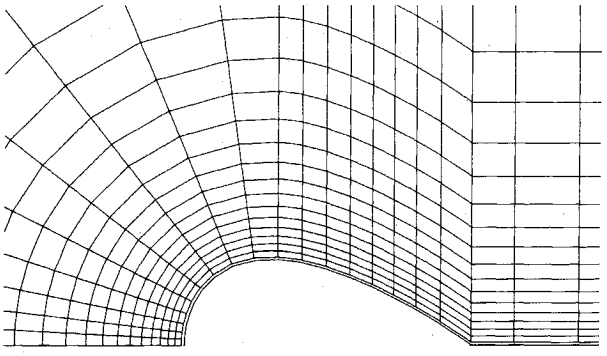

Fig. 1 Combined body-normal and sheared-cylindrical grid.

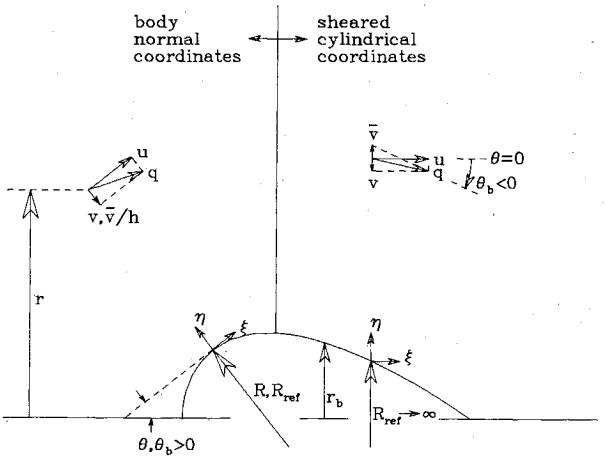

Fig. 2 Coordinate geometry and velocity component definition.

usual body-normal orientation for the reference body; and will, in fact, coincide with the directions S and N of Eq. (1) in regions where the grid is body-normal for the actual body.

Equation (1) is rewritten in more general form as

$$\bar{f}(\bar{\rho}\bar{u}\bar{r})_X + \bar{g}(\bar{\rho}\bar{v}\bar{r})_Y = 0 \tag{2}$$

which includes all the above specializations. With the aid of Fig. 2, the quantities used above are now defined.

$$\bar{f} = \frac{dX}{d\xi} \qquad 0 \le X(\xi) \le 1 \tag{3}$$

$$\bar{g} = \frac{dY}{d\eta} \qquad 0 \le Y(\eta) \le 1 \tag{4}$$

$$\bar{r} = r = r_b + \eta\cos\theta, \quad \text{for axisymmetric bodies}$$
$$= 1, \qquad \text{for planar two-dimensional bodies} \tag{5}$$

$$\bar{u} = \cos\theta + (1/h)\phi_\xi - r_b'\phi_\eta = \cos\theta + (\bar{f}/h)\phi_X - r_b'\bar{g}\phi_Y \tag{6}$$

$$\bar{v} = vh - r_b'\bar{u} \tag{7}$$

$$v = -\sin\theta + \phi_\eta = -\sin\theta + \bar{g}\phi_Y \tag{8}$$

$$r_b' = \tan(\theta_b - \theta) = 0, \qquad \text{body-normal grid}$$
$$= \tan\theta_b, \qquad \text{sheared grid} \tag{9}$$

$$h = 1 + K\eta, \qquad K = 1/R_{\text{ref}} \tag{10}$$

$$\bar{\rho} = \rho - \mu\rho_\sigma\Delta\sigma \tag{11}$$

$$\rho = (M_\infty^2 a^2)^{1/(\gamma-1)} \tag{12}$$

$$a^2 = \frac{1}{M_\infty^2} + \frac{\gamma-1}{2}(1-q^2) \tag{13}$$

$$q^2 = \bar{u}^2 + v^2 \tag{14}$$

$$\mu = \max(0, 1 - 1/M^2) \qquad \begin{matrix} \mu = 0, & M < 1 \\ 0 < \mu < 1, & M > 1 \end{matrix} \tag{15}$$

$$M = q/a \tag{16}$$

The stretch functions $\bar{f}$ and $\bar{g}$ are the derivatives of the computational coordinates with respect to the physical coordinates. The generalized radius $\bar{r}$ is appropriately defined for both axisymmetric and planar two-dimensional cases. The velocity components $\bar{u}$ and v are either in the usual body tangential and normal directions or are cylindrical components of velocity in sheared portions of the grid, where they are parallel and perpendicular to the reference body shape which is a cylinder. The physical contravariant η component of the total velocity is $\bar{v}$. A measure of the deviation of the actual body shape from the reference shape is given by r_b'. The metric h is unity in the sheared portions of the grid, since the reference surface has zero curvature in this region. However, R_{ref} is equal to the actual body radius of curvature R in body-normal regions of the mesh, so $h \to \infty$ as distance from the body increases. The artificial density is $\bar{\rho}$ and σ represents arc length along a streamline, which for many transonic cases closely corresponds to the tangential direction ξ in supersonic regions. In this development, the actual streamwise direction σ is replaced by ξ making for a simplified one-dimensional shifting of the density. The local speed of sound is a and the switch function μ is used to turn on the upwind density shift in supersonic flow regions.

Boundary Conditions

For the flow with a subsonic freestream, it is required that all perturbations vanish in the far field, as the flow approaches uniform conditions. Along the body surface, the component of velocity normal to the surface must vanish. Also, proper symmetry must be enforced, since the problem is solved only in the upper semi-infinite domain. For flow in a supersonic freestream, the same boundary conditions are employed, except that finite disturbances are allowed to propagate to downstream infinity in the sheared-cylindrical coordinates. These boundary conditions may be expressed in the following manner:

$$\phi = 0 \quad \text{as} \quad \eta \to \infty \tag{17}$$

$$\bar{v} = 0 \quad \text{at} \quad \eta = 0 \tag{18}$$

$$\phi_\xi = 0 \quad \text{at} \quad \xi = 0, \xi_{\max}; \text{ body-normal} \tag{19}$$

$$\phi_\xi = 0 \quad \text{as} \quad |\xi| \to \infty; \text{ sheared} \tag{20}$$

$$\phi(\xi_{\max}, \eta) \text{ extrapolated; sheared,} \quad M_\infty > 1 \tag{21}$$

Coordinate Stretching

The coordinate transformations, which map the physical variables ξ and η into the computational coordinates X and Y,

are similar to those used in the RAXBOD program.[2] Some modifications have been introduced which enhance accuracy and improve the versatility of the program.

Normal Direction

In the normal direction, the physical coordinate is related to the computational coordinate through a transformation of the form

$$\eta = AY/(1-Y)^{\alpha} \tag{22}$$

where the parameters A and α can be used to adjust mesh density both near the body and in the far field. This is identical to the transformation used in RAXBOD. As previously mentioned, the normal and computational coordinates are zero at the body surface. As the computational coordinate approaches unity, the normal coordinate η approaches infinity.

Tangential Direction

For closed, blunt-nosed bodies, the physical arc length along the body, in the range $0 \le \xi \le \xi_{max}$, is mapped into the computational region $0 \le X \le 1$. In the RAXBOD program, this was accomplished through a polynomial transformation. In this conservative version, a new closed-body coordinate stretching in the tangential direction has been introduced which allows for better resolution in the nose and tail regions of slender, blunt bodies like a 10:1 ellipse. A truncated hyperbolic tangent function of the form

$$\xi = \left[\frac{\xi_{max}}{2}\tanh(2X-1) + \frac{\xi_{max}}{2}\tanh(1)\right] \Big/ \tanh(1)$$

$$0 \le X(\xi) \le 1 \tag{23}$$

is used to map the physical arc length into the computational region. This stretching can provide nearly uniform spacing over the majority of the body, with high grid density near the high curvature nose and tail regions where large flow gradients occur.

For bodies on a sting ("open" bodies) or for airfoil shapes, body-normal coordinates may be appropriate near the nose, but for other regions may provide poor resolution. Also, for concave shapes, the body-normal coordinate lines intersect, making proper discretization of the problem impossible. In RAXBOD, a combined body-normal and sheared-cylindrical coordinate system, joined at the body station having the most upstream horizontal tangent, was used for open bodies. This option has been extended to include closed-body shapes, such as shown in Fig. 1. Thus, proper discretization can be achieved at both the leading and trailing edges of airfoil- or torpedo-like shapes, where the forebody is blunt and the tail ends in a wedge or point.

The stretching used for the combined body-normal and sheared-cylindrical coordinate systems is identical to that used in RAXBOD, since this particular stretching provides a great deal of freedom in grid spacing for two different areas of the body. The physical coordinate ξ is related to the computational coordinate X by a polynomial expression of the form

$$\xi = AX + BX^3 + CX^5 + DX^7 \qquad 0 \le X \le X_M \tag{24}$$

for the upstream portion. In the downstream portion of the mesh, an expression of the form

$$\xi = \xi_M + [E(X-X_M)(1-X_M)]/(1-X) \quad X_M \le X \le 1 \tag{25}$$

is used to relate the physical and computational coordinates. The coefficients in Eqs. (24) and (25) are determined, exactly as in RAXBOD, from the condition that the computational coordinate and its first two derivatives be continuous at the matching point ξ_M. Also specified are the stretch derivatives at the nose and the matching point.

The combined body-normal and sheared-cylindrical grid option was further extended to a fully-sheared cylindrical grid to be used with bodies having a pointed nose and pointed or open tail. The sheared-cylindrical grid extends to upstream and downstream infinity, with the "normal" lines perpendicular to the axis of symmetry.

It should be noted that the combined body-normal and sheared-cylindrical grid will have discontinuous metrics along the entire interface line between the two grids and along any radial line extending from the near neighborhood of a surface slope or curvature discontinuity. No special treatment of these discontinuities has been provided in the present conservative formulation, nor in the previous nonconservative RAXBOD formulation; although significant, nonphysical effects can occur in solutions obtained from either method. In subsonic regions these effects should dissipate very quickly and have minimal impact. In supersonic regions, however, the metric jumps due to slope and curvature discontinuities propagate along characteristic lines essentially undiminished and can influence the entire solution. It is not possible to assess completely what specific effects are present in solutions for cases having such discontinuities, although certain effects described later are more noticeable when a sonic line crosses a line of metric discontinuity. Generally speaking, for bodies with slope and/or curvature discontinuities, coordinate systems based on conformal[8] or elliptic-mapping[9] ideas should be used, since they have the capability to isolate singularities at the boundaries.

Computational Procedure

Finite Difference Approximation

A finite difference analog to the generalized continuity equation (2) and its accompanying boundary conditions, Eqs. (17-21), is set up. Emphasis is placed on maintaining global conservation of mass throughout the discretization process. The resulting finite difference equations are solved numerically using an iterative technique which approaches the exact discretized solution for a particular grid. Mesh refinement and reasonable levels of convergence allow the discrete approximation to approach a solution to the problem with acceptable accuracy.

Interior Field Points

The finite difference approximation to the generalized continuity equation can be written as

$$R_{ij} = f_i[(\bar{\rho}\bar{u}\bar{r})_{i+\frac{1}{2},j} - (\bar{\rho}\bar{u}\bar{r})_{i-\frac{1}{2},j}] + g_j[(\bar{\rho}\bar{v}\bar{r})_{i,j-\frac{1}{2}} - (\bar{\rho}\bar{v}\bar{r})_{i,j+\frac{1}{2}}] = 0 \tag{26}$$

which is correct to second order, i.e., $0(\Delta X^2 + \Delta Y^2)$, at subsonic points where the density evaluation is not shifted upwind. Here, i is the tangential direction index which increases as the computational coordinate X varies from zero to one. The normal direction index is j which decreases as the computational coordinate Y increases; i.e., $j=1$ is at the outer boundary. The metrics f_i and g_j are the same as those defined by Eqs. (3) and (4) except they are divided by ΔX and ΔY, respectively, and evaluated at the point (ij). The flow variables $\bar{\rho}, \bar{u}, \bar{v}$, and the generalized radius $\bar{r}$, are evaluated in the usual central-differencing molecule. A typical portion of the computational mesh is shown in Fig. 3 to detail where the flow variables are computed as follows.

The computational procedure is: Initially, an approximation to the disturbance potential (for example, interpolated values from a coarser mesh) is given at each interior node point. Values for the disturbance potential at ghost points are then set to satisfy the proper symmetry or

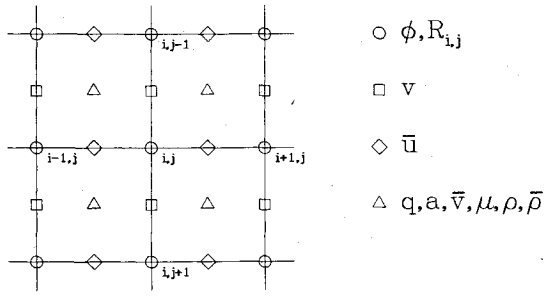

Fig. 3 Flow variables at interior mesh points.

body-boundary conditions, as described subsequently. The velocity components $\bar{u}$ and v are then evaluated at midsegments of mesh lines as

$$\bar{u}_{i+\frac{1}{2},j} = (\cos\theta)_{i+\frac{1}{2}} + (f/h)_{i+\frac{1}{2},j}(\phi_{i+1,j} - \phi_{ij}) - (r_b' g \phi_Y)_{i+\frac{1}{2},j} \tag{27}$$

$$v_{i,j+\frac{1}{2}} = (\sin\theta)_i + g_{j+\frac{1}{2}}(\phi_{ij} - \phi_{i,j+1}) \tag{28}$$

Geometric variables such as $(\cos\theta)_{i+\frac{1}{2}}$ and $(r_b')_{i+\frac{1}{2}}$ can be obtained by averaging neighboring values, known at grid line intersections with the body surface by a spline fit or from an analytic expression for the body shape. The normal gradient $(\phi_y)_{i+\frac{1}{2},j}$ is obtained by averaging centered differences of ϕ at i and $i+1$, each computed over two cell heights. A cell-centered total velocity is computed from Eq. (14) by averaging the $\bar{u}$ and v components on surrounding mesh segments. Also cell-centered speeds of sound, isentropic densities, and switch functions are computed from Eqs. (13), (12), and (15), respectively. The metrics $\bar{r}$, h, f, and g in Eqs. (26-28) are evaluated either directly from their corresponding analytic equations or by averaging neighboring values at the appropriate midsegment or node points.

For many transonic cases, the supersonic streamlines can be assumed to coincide with lines of $Y=$const and in the direction of increasing X. For this reason, as mentioned previously, a simplified, unidirectional shifting scheme is used in computing the artificial density which accounts for the predominant density gradient in the X direction. The artificial density is computed at the midcell as

$$\tilde{\rho}_{i+\frac{1}{2},j+\frac{1}{2}} = \rho_{i+\frac{1}{2},j+\frac{1}{2}} - \mu_{i,j+\frac{1}{2}}(\rho_{i+\frac{1}{2},j+\frac{1}{2}} - \rho_{i-\frac{1}{2},j+\frac{1}{2}}) \tag{29}$$

which shifts the density evaluation upstream in the tangential direction. Values for the switch function $\mu_{i,j+\frac{1}{2}}$ are obtained by averaging two adjacent cell-centered switch functions. Similarly, midsegment shifted densities, such as $\tilde{\rho}_{i+\frac{1}{2},j}$ in Eq. (26), are obtained by averaging neighboring midcell artificial densities. The residuals are then computed at each node point and the solution to the set of finite difference equations is obtained iteratively as described subsequently.

Half-Cell Mesh Structure

In order to facilitate the application of the flow-tangency boundary condition along the body surface given by Eq. (18) and the Neumann conditions given by Eqs. (19) and (20), a "ghost-point" method is used in which some mesh coordinates are located outside the domain of interest. The ghost-point method was also used in RAXBOD; although, in the conservative procedure described here, appropriate modifications are made to achieve improved accuracy and stability.

In RAXBOD, the body surface coincided with the coordinate line $\eta=0$ and the ghost-point line was placed inside the body. A central difference approximation to the normal derivative of the disturbance potential was made over two cell heights, between the line immediately above the body surface and the ghost line inside the body. In the present version, the "half-cell" approach is used, whereby the body surface is in the middle of the computational cells. Thus, the normal partial derivatives required in the difference operator and in the body-boundary condition are approximated by differences over just one cell height. Smaller truncation errors occur then in application of the body-boundary condition. This cell structure is the natural one for the conservative potential equation with Neumann boundary conditions.

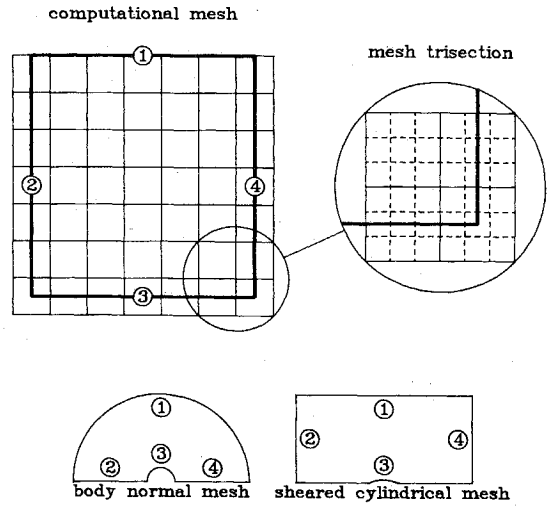

Fig. 4 Computational mesh and grid refinement technique.

Along the axis of symmetry, which is a streamline and can be thought of as an extension of the actual body surface, a similar ghost-point method is also used to enforce the symmetry condition there. Along this axis, however, the ghost points are used to enforce the symmetry condition in the tangential direction for body-normal coordinates, as given in Eq. (19), or in the normal direction for the sheared-cylindrical coordinates. It should be noted that this half-cell mesh structure obviates the need for special limiting equations at the axis of symmetry, such as those used in RAXBOD.[1]

In the sheared-cylindrical coordinates, where ξ ranges from negative to positive infinity, the ghost-point method is also used to enforce the far-field condition given by Eq. (20). Here, the ghost points are used to enforce zero-gradient Neumann conditions, equivalent to the condition that the flow must approach uniform flow far from the body.

The method of mesh refinement was necessarily modified in order to remain consistent with the half-cell mesh structure on three sides of the computational plane. A mesh trisection technique is used, which on the refined grid places two equally spaced coordinate lines between existing coarse mesh lines. The half-cell structure and mesh trisection technique are illustrated in Fig. 4.

Z Scheme for Body-Boundary Condition

At symmetry or far-field boundaries, the value of the disturbance potential for ghost points is set equal to the adjacent value on the interior of the domain. Ghost values for the body-boundary condition are set using a tridiagonal method which may be called the "Z scheme," which seems to be an improvement over the usual approach when the coordinates are nonorthogonal at the boundary. From Eqs. (18) and (6-9) it can be shown that the body-boundary condition is equivalent to

$$1 + r_b'^2 \phi_\eta = \sin\theta + r_b'(\cos\theta + \phi_\xi) \tag{30}$$

from which

$$\phi_\eta = \cos(\theta_b - \theta)\sin\theta_b + \tfrac{1}{2}\sin[2(\theta_b - \theta)]\phi_\xi \tag{31}$$

The partial derivative ϕ_ξ is then evaluated at the point $(i,j_{\max}+\frac{1}{2})$ using finite differences above and below the surface in such a way that there results a diagonally-dominant, tridiagonal system for the ghost values:

$$A_i\phi_{i+1,j_{\max}+1}+B_i\phi_{i,j_{\max}+1}+C_i\phi_{i-1,j_{\max}+1}=D_i \tag{32}$$

where

$$A_i=\tfrac{1}{4}(b_i-|b_i|)f_i/g_{j_{\max}+\frac{1}{2}} \tag{33a}$$

$$B_i=1+\tfrac{1}{2}|b_i|f_i/g_{j_{\max}+\frac{1}{2}} \tag{33b}$$

$$C_i=-\tfrac{1}{4}(b_i+|b_i|)f_i/g_{j_{\max}+\frac{1}{2}} \tag{33c}$$

$$D_i=-a_i/g_{j_{\max}+\frac{1}{2}}+A_i\phi_{i-1,j_{\max}}+B_i\phi_{ij_{\max}}+C_i\phi_{i+1,j_{\max}} \tag{33d}$$

and

$$a_i=[\cos(\theta_b-\theta)\sin\theta_b]_i \tag{34a}$$

$$b_i=\{\tfrac{1}{2}\sin[2(\theta_b-\theta)]\}_i \tag{34b}$$

The resulting system thus involves in sheared coordinates only the points $(i-1,j_{\max})$, $(i,j_{\max})$, $(i,j_{\max}+1)$, and $(i+1,j_{\max}+1)$ which resembles a Z shape when θ_b, and hence b_i, is less than zero. The computation molecule has the reverse shape if $b_i>0$. The tridiagonal system has Dirichlet boundary conditions on both ends, where we set $\phi_{i,j_{\max}+1}=\phi_{i,j_{\max}}$ for $i=1$ or $i_{\max}$.

Freestream Tare Residual

A particular discrete analog of the conservative mass equation does not necessarily satisfy uniform flow with a zero residual at interior points. In fact, far from the body, the residuals can be very large due to the truncation errors and the large cell volumes. These errors can cause, in some cases, catastrophic instability or, at least, large errors in the final solution. There are several ways of overcoming this difficulty, but one of the simplest and most effective was suggested to the authors by Steger.[10] The idea is to evaluate the interior residuals obtained by substituting in the freestream condition (taking care to allow the body to be a flow-through surface for this purpose) and to subtract this "freestream tare" residual from the right-hand side. The resulting difference operator thus satisfies uniform flow with zero error. Our implementation of this feature can be written thus, where R_{ij} is replaced by

$$R_{ij}=f_i\{[\bar{r}(\bar{\rho}\bar{u}-\bar{\rho}_\infty\bar{u}_\infty)]_{i+\frac{1}{2},j}-r[(\bar{\rho}\bar{u}-\bar{\rho}_\infty\bar{u}_\infty)]_{i-\frac{1}{2},j}\}$$
$$+g_j\{[\bar{r}(\bar{\rho}\bar{v}-\bar{\rho}_\infty\bar{v}_\infty)]_{i,j-\frac{1}{2}}-[\bar{r}(\bar{\rho}\bar{v}-\bar{\rho}_\infty\bar{v}_\infty)]_{i,j+\frac{1}{2}}\} \tag{35}$$

Use of this procedure allowed accurate solution of classical check cases such as incompressible flow over spheres and circles.

Iterative Algorithm

The collection of finite difference equations at interior and boundary points is solved by a successive vertical-line over-relaxation scheme. The disturbance potential is updated by solving simultaneously $X=$const lines, proceeding in the direction of increasing X. In this method we used the "simple" SLOR scheme previously described in Ref. 7, whereby the iteration coefficients (coefficients of $\Delta\phi_{ij}=\phi_{ij}^{N+1}-\phi_{ij}^{N}$) depend only on the spatially-varying metrics; the residual right-hand side is "scaled" by dividing by an average density. New values of $\phi_{i-1,j}$ are inserted by adding appropriate terms involving $\Delta\phi_{i-1,j}$ to the right-hand side. In the event that additional amounts of iterative damping[11] are required for difficult cases, a term $\beta\phi_{X_t}$ is easily handled.[7] The SLOR scheme, however, already has an excess margin of "natural" ϕ_{X_t}, which is sufficient for stable iterations in most cases.

Results

Conservative solutions are compared to nonconservative, full-potential results obtained from a version of the RAXBOD code. The RAXBOD code has been compared[1] directly to experimental data for many cases of interest; thus, no direct comparisons between conservative solutions and experimental data are presented in this paper. It is expected that good agreement with unseparated experimental data will be obtained when the conservative method is interacted correctly with a viscous code, as shown in Ref. 3.

For cases in which the flowfield is completely subsonic and particularly for incompressible ($M_\infty=0.001$) flows, the

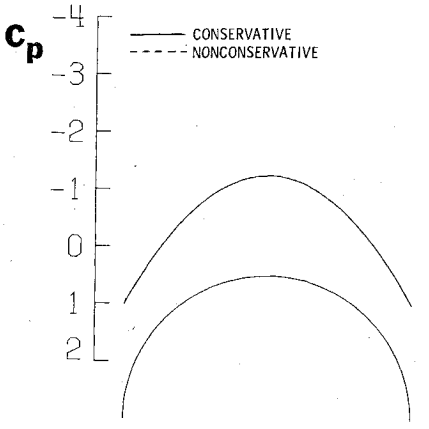

Fig. 5 Pressure coefficient for sphere in incompressible ($M_\infty=0.001$) flow.

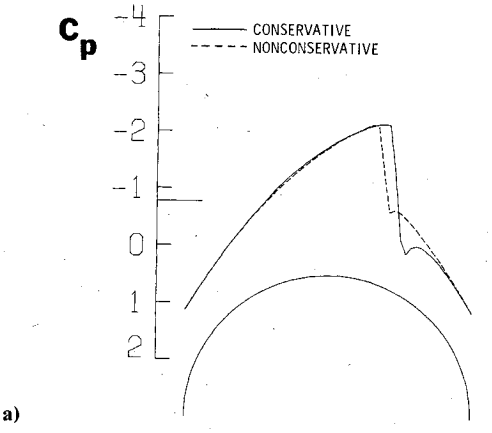

a)

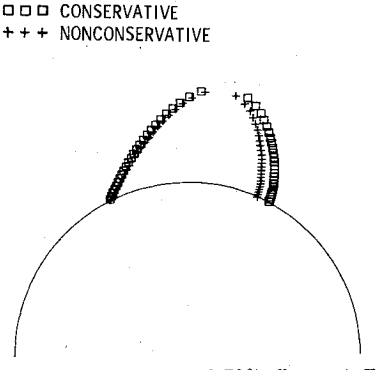

b)

Fig. 6 Sphere in transonic ($M_\infty=0.700$) flow. a) Pressure coefficient. b) Sonic line.

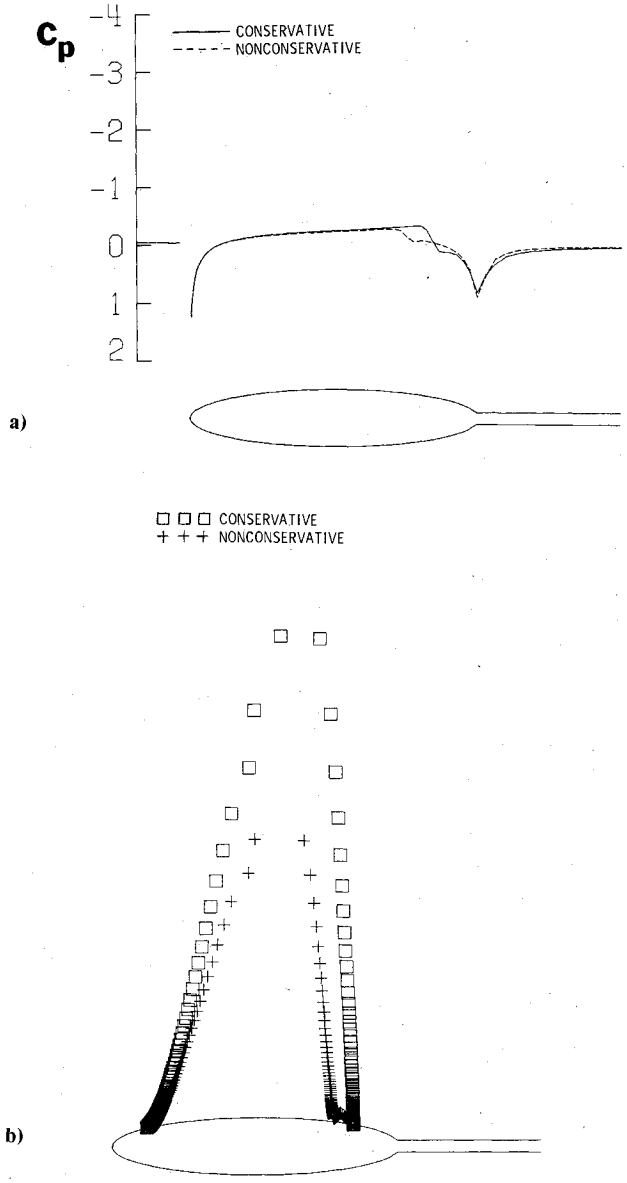

Fig. 7 Ellipsoid on sting in transonic ($M_\infty = 0.970$) flow. a) Pressure coefficient. b) Sonic line.

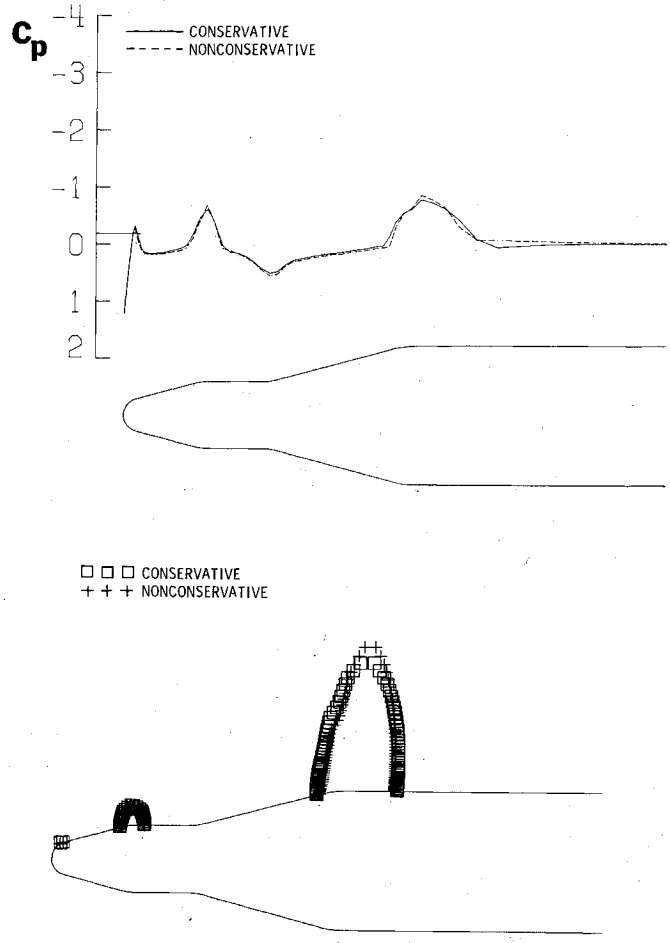

Fig. 8 Missile forebody in transonic ($M_\infty = 0.900$) flow. a) Pressure coefficient. b) Sonic line.

conservative and nonconservative full-potential solutions are identical at convergence. Specifically, with sufficiently low freestream Mach numbers, it is possible to duplicate the exact incompressible solutions for bodies like the sphere and cylinder, in both the conservative and nonconservative programs. Figure 5 shows the incompressible solution for a sphere.

In transonic cases, with shocks present, noticeable differences appear between the conservative and nonconservative full-potential solutions. For example, Fig. 6 shows the body pressure coefficient and sonic line in transonic ($M_\infty = 0.7$) flow. As expected, the shock strength for the conservative solution is much greater than that of the nonconservative solution. The conservative shock is nearly symmetric about the sonic pressure coefficient level, which is indicated by the large tic on the C_p axis. The nonconservative shock just reaches the sonic pressure coefficient level. Also, the conservative shock is farther downstream than the nonconservative shock. This is further emphasized by the larger supersonic region shown in Fig. 6b for the conservative method.

Figure 7 shows results for an ellipsoid on a sting in transonic ($M_\infty = 0.97$) flow. The comparison is similar to the previous figure, in that the conservative shock is stronger, more symmetric about the sonic pressure coefficient level, and farther downstream relative to the nonconservative solution. Notice the large supersonic regions, particularly for the conservative solution.

Figure 8 shows a more practical axisymmetric case, that of a typical missile forebody. At this Mach number ($M_\infty = 0.9$), the conservative and nonconservative full-potential solutions are almost identical, even though there are three distinct supersonic regions. For slightly higher freestream Mach numbers, the differences become much more evident and follow the trends mentioned above.

In contrast, Fig. 9 shows widely different solutions for a planar two-dimensional circular arc airfoil at $M_\infty = 0.92$. The nonconservative solution has a normal shock at the trailing edge. The conservative full-potential solution has an oblique shock at the trailing edge, with a normal shock terminating the supersonic region approximately one chord length downstream of the airfoil. This case employed the sheared-cylindrical grid option to provide better resolution at the leading and trailing edges than is possible with body-normal coordinates.

As mentioned earlier, there are significant effects due to the metric discontinuities of the combined body-normal and sheared-cylindrical grid. Of these, the most noticeable effect can be seen in Figs. 7b, 8b, and 9b. The sonic lines for these conservative and nonconservative solutions have inflection points in the vicinity of a slope or curvature discontinuity. Solutions like these, obtained using the present method, have also been compared to solutions from programs which have no metric discontinuities. These comparisons revealed somewhat smaller supersonic regions and slightly reduced peak Mach numbers for the solutions obtained on grids

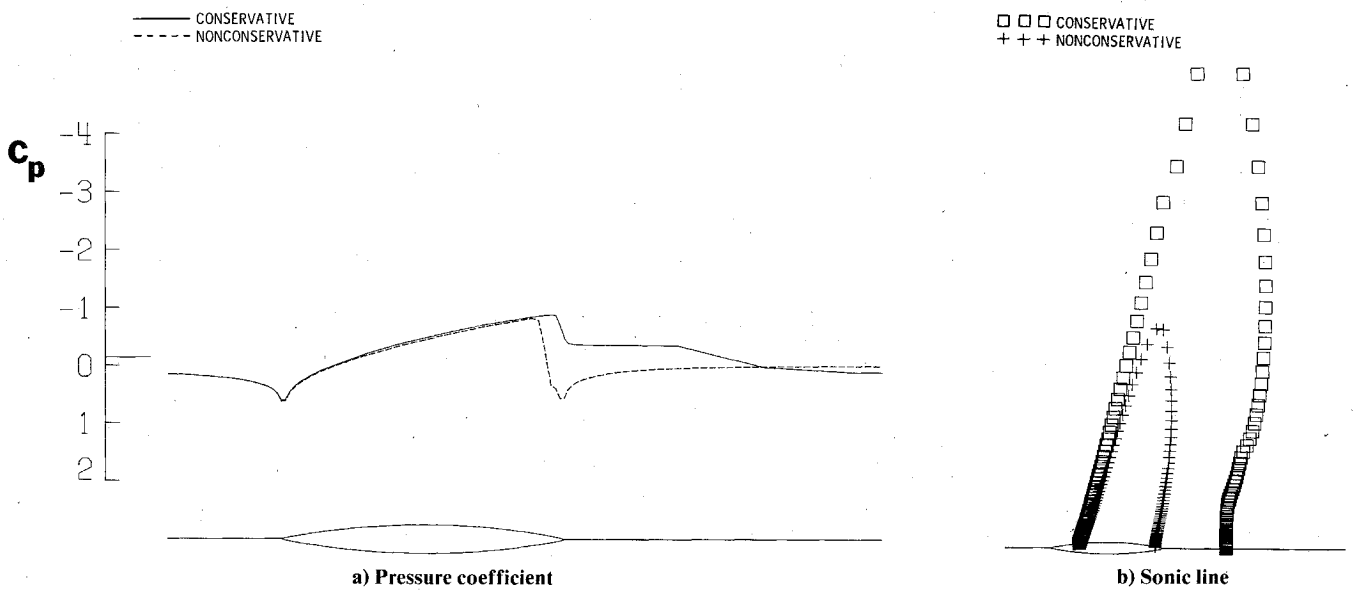

a) Pressure coefficient b) Sonic line

Fig. 9 Circular arc airfoil in transonic ($M_\infty = 0.920$) flow.

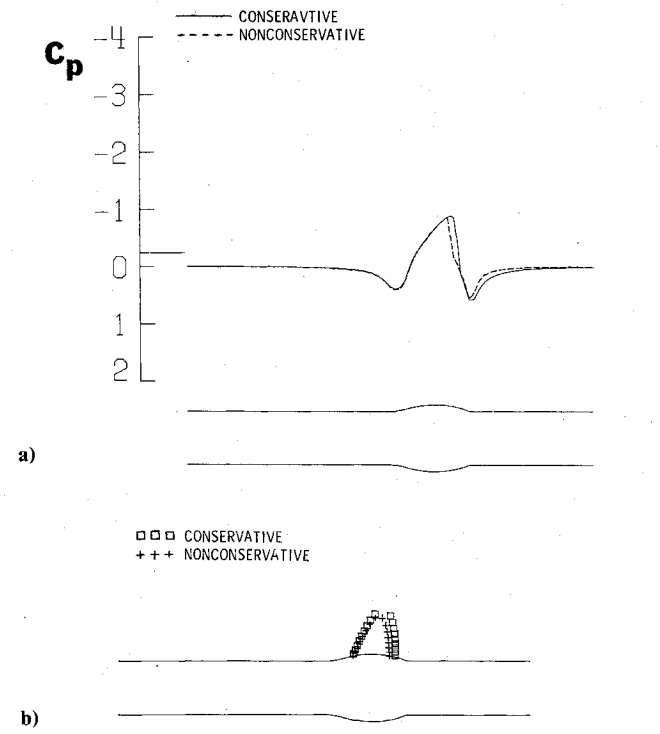

Fig. 10 Axisymmetric bump on pipe (Bachalo-Johnson body) in transonic ($M_\infty = 0.875$) flow. a) Pressure coefficient. b) Sonic line.

having metric discontinuities. There may be other effects of metric jumps on a particular solution, but at least the size and shape of supersonic regions which cross slope and/or curvature discontinuities are influenced.

Figure 10 shows an axisymmetric body with an "open" nose (actually represents a bump on a pipe) in a transonic ($M_\infty = 0.875$) flow. The body[12] is assumed to extend infinitely upstream and downstream, with undisturbed flow ahead of the bump. In the shock region, similar differences exist between the conservative and nonconservative solutions as mentioned previously. The conservative shock is stronger, nearly symmetric about the sonic pressure coefficient level, and farther downstream relative to the nonconservative shock.

Conclusion

After accounting for the freestream tare residual, the conservative full-potential formulation agrees, at convergence, perfectly with the nonconservative procedure for incompressible flows. The full-potential formulation (minus tare) allows known incompressible solutions for bodies such as the sphere and cylinder to be computed accurately. A tridiagonal "Z scheme" proved effective for implementing Neumann boundary conditions in nonorthogonal coordinates. In transonic flow, the artificial compressibility method affords a convenient means for introducing artificial viscosity. As expected, noticeable differences exist between conservative and nonconservative full-potential solutions due to treatment of shocks present in the flowfield. The conservative shocks tend to be stronger and more symmetric about the sonic level pressure coefficient, relative to the nonconservative results. Additionally, the shock location occurs farther downstream in the conservative solution than is calculated by the nonconservative program. As a final point, it should be noted that the conservative formulation entails considerably more computational work per iteration than the nonconservative method, but both have nearly the same asymptotic convergence rate.

References

[1]South, J. C. Jr. and Jameson, A., "Relaxation Solutions for Inviscid Axisymmetric Transonic Flow Over Blunt or Pointed Bodies," *Proceedings of AIAA Computational Fluid Dynamics Conference*, Palm Springs, Calif., July 1973, pp. 8-17.

[2]Keller, J. D. and South, J. C. Jr., "RAXBOD: A Fortran Program for Inviscid Transonic Flow Over Axisymmetric Bodies," NASA TM X-72831, Feb. 1976.

[3]Melnik, R. E., "Wake Curvature and Trailing-Edge Interaction Effects in Viscous Flow Over Airfoils," NASA CP 2045, Pt. I, Vol. 1, March 1978, pp. 255-270.

[4]Lax, P. and Wendroff, B., "Systems of Conservation Laws," *Communications on Pure and Applied Mathematics*, Vol. XIII, May 1960, pp. 217-237.

[5]Newman, P. A. and South, J. C. Jr., "Influence of Nonconservative Differencing on Transonic Streamline Shapes," *AIAA Journal*, Vol. 14, Aug. 1976, pp. 1148-1149.

[6]Holst, T. L., "An Implicit Algorithm for the Conservative, Transonic Full-Potential Equation Using an Arbitrary Mesh," AIAA Paper 78-1113, July 1978.

[7]Hafez, M. M., South, J. C. Jr., and Murman, E. M., "Artificial Compressibility Methods for Numerical Solution of Transonic Full-Potential Equation," AIAA Paper 78-1148, July, 1978.

[8]Davis, R. T., "Methods for Coordinate Generation Based on Schwarz-Christoffel Transformation," *Proceedings of AIAA Computational Fluid Dynamics Conference*, Williamsburg, Va., July 1979, pp. 180-194.

[9]Thompson, J. F., Thames, F. C., and Mastin, C. W., "Automatic Numerical Grid Generation of Body Fitted Curvilinear Coordinate System for Field Containing Any Arbitrary Number of Two-Dimensional Bodies," *Journal of Computational Physics*, Vol. 15, July 1974, pp. 299-319.

[10]Steger, J. L. and Caradonna, F. X., "A Conservative Implicit Finite-Difference Algorithm for the Unsteady Transonic Full-Potential Equation," Flow Simulation, Inc., Rept. 79-04 for U.S. Army Aeromechanics Lab., NASA Contract NAS2-10417, Dec. 1979.

[11]Jameson, A., "Iterative Solution of Transonic Flows Over Airfoils and Wings, Including Flows at Mach 1," *Communications on Pure and Applied Mathematics*, Vol. 27, May 1974, pp. 283-309.

[12]Bachalo, W. D. and Johnson, D. A., "An Investigation of Transonic Turbulent Boundary Layer Separation Generated on an Axisymmetric Flow Model," AIAA Paper 79-1479, July 1979.